Coulomb stress changes caused by repeated normal faulting earthquakes during the 1997 Umbria-Marche (central Italy) seismic sequence

Concetta Nostro, Lauro Chiaraluce, and Massimo Cocco
Istituto Nazionale di Geofisica e Vulcanologia, Rome, Italy

David Baumont and Oona Scotti
Institut de Radioprotection et de Suretè Nuclèaire, Fontenay-Aux-Roses, France

Received 13 August 2004; revised 2 March 2005; accepted 1 April 2005; published 25 May 2005.

[1] We investigate fault interaction through elastic stress transfer among a sequence of moderate-magnitude main shocks ($5 < M_w < 6$) which ruptured distinct normal fault segments during a seismic sequence in the Umbria-Marche region (central Apennines). We also model the spatial pattern of aftershocks and their faulting mechanisms through Coulomb stress changes. We compute stress perturbations caused by earthquake dislocations in a homogeneous half-space. Our modeling results show that seven out of eight main shocks of the sequence occur in areas of enhanced Coulomb stress, implying that elastic stress transfer may have promoted the occurrence of these moderate-magnitude events. Our modeling results show that stress changes caused by normal faulting events reactivated and inverted the slip of a secondary N-S trending strike-slip fault inherited from compressional tectonics in its shallowest part (1–3 km). Of the 1517 available aftershocks, 82% are located in areas of positive stress changes for optimally oriented planes (OOPs) for Coulomb failure. However, only 45% of the 322 available fault plane solutions computed from polarity data is consistent with corresponding focal mechanisms associated with the OOPs. The comparison does not improve if we compute the optimally oriented planes for Coulomb failure by fixing the strike orientation of OOPs using information derived from structural geology. Our interpretation of these modeling results is that elastic stress transfer alone cannot jointly explain the aftershock spatial distribution and their focal mechanisms.

Citation: Nostro, C., L. Chiaraluce, M. Cocco, D. Baumont, and O. Scotti (2005), Coulomb stress changes caused by repeated normal faulting earthquakes during the 1997 Umbria-Marche (central Italy) seismic sequence, *J. Geophys. Res.*, *110*, B05S20, doi:10.1029/2004JB003386.

1. Introduction

[2] Coulomb stress changes are widely used in the literature to investigate fault interaction between large-magnitude earthquakes as well as to model aftershock patterns and seismicity rate changes over long time windows [see *Harris*, 1998; *Stein*, 1999; *King and Cocco*, 2001; *Toda and Stein*, 2003, and references therein]. Among the numerous papers published in the literature, only a few studies explore fault interaction in extensional tectonic settings [see, e.g., *Hodgkinson et al.*, 1996; *Nostro et al.*, 1997; *Caskey and Wesnousky*, 1997; *Troise et al.*, 1998; *Nalbant et al.*, 1998; *Belardinelli et al.*, 1999; *Papadimitriou and Sykes*, 2001]. *Cocco et al.* [2000] modeled the static stress changes caused by several normal faulting events that occurred in 1997 in the Umbria-Marche region (central Apennines). This sequence of moderate-magnitude earthquakes is extremely interesting because it is characterized by the progressive activation of adjacent and nearby parallel fault segments belonging to a complex normal fault system (see Figure 1 and *Chiaraluce et al.* [2003]) and by a migration of seismicity along the strike of the main faults from NW toward SE (see Figure 2a and *Deschamps et al.* [2000] and *Chiaraluce et al.* [2004]). In the present study, we investigate the 1997 Umbria-Marche sequence with the goal of modeling through elastic stress transfer the whole pattern of seismicity (main shocks and aftershocks).

[3] The main motivation of this research is to make use of detailed new information, which includes very accurate earthquake locations for main shocks and aftershocks [*Chiarabba and Amato*, 2003; *Chiaraluce et al.*, 2003], aftershocks fault plane solutions [*Chiaraluce et al.*, 2004] and the slip distributions imaged for the three largest earthquakes of the sequence [*Hernandez et al.*, 2004]. The fault geometry of the largest-magnitude ($M > 5$) earthquakes and the regional tectonic stress tensor have

0148-0227/05/2004JB003386$09.00

been constrained by analyzing centroid moment tensor (CMT) fault plane solutions [*Ekström et al.*, 1998], aftershock hypocenters and *P* wave polarity data [*Chiaraluce et al.*, 2003, 2004]. This provides a unique opportunity to test whether the aftershock locations and focal mechanisms are consistent with the elastic stress perturbations caused by subsequent earthquake dislocations in an extensional tectonic setting.

[4] *Cocco et al.* [2000] concluded that elastic stress perturbations promoted subsequent earthquake failures during the 1997 Umbria-Marche sequence; in particular, the locations and geometry of the three largest events of this sequence ($M_w \geq 5.6$) are consistent with the calculated Coulomb stress changes. However, they were unable to model the whole sequence of earthquakes with $M_w \geq 5$ (see Figure 2a) in terms of static stress changes. These authors stated that normal faulting aftershocks located on the hanging wall and at close distances from the main shock rupture planes always lie in a stress shadow zone. In other words, Coulomb static stress changes cannot explain the presence of normal faulting events on the hanging wall of the main shock planes. *Cocco et al.* [2000] have also shown that normal stress changes better agree with the spatial pattern of main shock locations, suggesting that fluid flow may play an important role in promoting earthquakes. This issue has been further investigated by *Antonioli et al.* [2005], who modeled the southeastward migration of seismicity during the Umbria-Marche sequence as the pore pressure relaxation in a fractured poroelastic fluid-saturated medium. The resulting values of diffusivity are consistent with observations in other tectonic areas [*Noir et al.*, 1997; *Shapiro et al.*, 2003] and the inferred direction of fluid flow coincides with the average strike of the rupture planes. This is consistent with the observation that seismicity migrated along the strike direction at an apparent velocity of 1 km/d [see also *Miller et al.*, 2004]. The presence of seismicity on the hanging wall of the main fault system (see Figure 1) has been interpreted by *Miller et al.* [2004] to be driven by a pressure pulse originating (coseismically) from a known deep source of trapped high-pressure CO_2 [*Chiodini et al.*, 2000] and propagating into the damage region created at the time of the earthquake. All these investigations demonstrate that both elastic interactions and fluid flow play an important role during the 1997 Umbria-Marche sequence. These results encourage us to perform a detailed modeling of main shocks and aftershocks patterns through Coulomb stress changes using the new results and information.

2. Seismic Sequence

[5] We first summarize the main features of the 1997 Umbria-Marche earthquake sequence, which we model in this study. Several moderate-magnitude earthquakes ($5 < M_w < 6$) ruptured normal fault segments of the southern sector of the North Apennine belt (central Italy). Their hypocentral locations, magnitude and fault plane solutions are listed in Table 1 and shown in Figure 2a. The progressive activation of these 5 to 12 km long segments made up a broad, ~45 km long, NW trending fault system (Figures 1 and 2a). The geometry of each segment is quite simple and consists of planar faults gently dipping toward SW with an average dip of 40°–45° [*Amato et al.*, 1998; *Chiaraluce et al.*, 2003]. The fault planes maintain a constant dip through the entire seismogenic volume, down to 8 km depth. We observe the activation of faults in the hanging wall and the absence of seismicity in the footwall of the structure (Figure 1). *Chiaraluce et al.* [2003] and *Chiarabba and Amato* [2003] attribute the observed fault segmentation to the lateral heterogeneity of the upper crust: preexisting thrusts inherited from Neogene compressional tectonics intersect the active normal faults and control their maximum length (see Figure 1). The N-S lateral termination of these compressional structures have been mapped at the surface as right-lateral minor transfer faults, which are not consistent with the present-day active stress field [*Collettini et al.*, 2005]. The stress tensor obtained by *Chiaraluce et al.* [2003] inverting the focal mechanisms of the six largest-magnitude events of the 1997 sequence is in agreement with the tectonic stress active in the inner chain of the Apennine [*Mariucci et al.*, 1999; *Lavecchia et al.*, 1994], revealing a clear NE trending extension direction: trend and plunge of the principal axes are listed in Table 2.

[6] The aftershock focal mechanisms are very similar to the associated main shock solution. The available 322 aftershock focal mechanisms show a consistent extensional kinematics, 70% of which reveals normal faulting and 24% are associated with left-lateral strike-slip events [*Chiaraluce et al.*, 2004]. For the largest-magnitude earthquakes of the 1997 sequence, we use in this paper the fault geometry proposed by *Chiaraluce et al.* [2003, 2004] (see Figure 2a), based on the spatial distribution of 1517 relocated aftershocks ($2.5 \leq M < 6$) having formal location errors of tens of meters, the slip patterns proposed by *Hernandez et al.* [2004] for the three largest events (obtained by inverting GPS, DInSAR, and strong motion data) and the rupture directivity estimated by *Pino et al.* [1999]. We also include in our analysis the Gualdo Tadino earthquake that occurred on 3 April 1998 at the northwestern edge of the activated seismogenic volume (event 9 in Figure 2a). For all the main events we use the CMT focal mechanisms proposed by *Ekström et al.* [1998], except that for the 6 October 1997 event for which we also use the focal mechanism (event 5b in Figure 2a) calculated by *Chiaraluce et al.* [2003] from *P* wave polarity data (the CMT fault plane solution for this event was used by *Cocco et al.* [2000]). The largest shocks of the sequence nucleated near the base of the seismogenic volume (5–6 km) and propagate nearly unilaterally and updip (see Figure 1).

[7] Each large event had its own aftershock sequence (see Figure 2b) with a usual temporal decay described by an Omori law. Nonetheless, Figure 2b points out the peculiar temporal evolution of seismicity and the fluctuations of the rate of earthquake production during the sequence. Unfortunately, we cannot evaluate the changes in seismicity rate in the study area, because we cannot estimate the background rate and measure its spatial variability due to the poor resolution of the available seismic catalogue. Earthquakes investigated in this study have been recorded by a temporary seismic network deployed after 26 September 1997. Therefore we cannot attempt to investigate the correlation between Coulomb stress and seismicity rate changes. *Console et al.* [2000] found that the investigated area had been characterized by a quiescence preceding the September 1997 main shocks, but

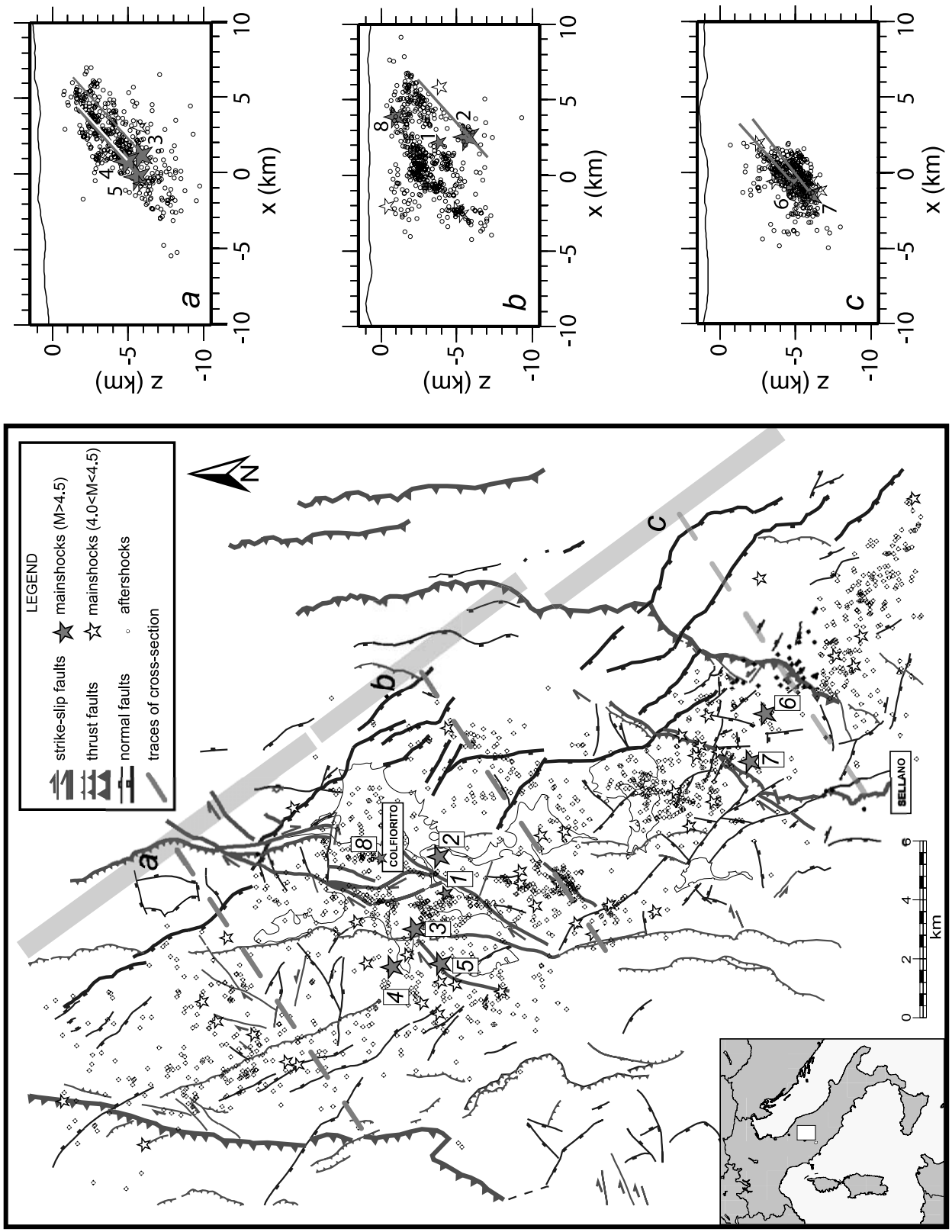
LEGEND
strike-slip faults
thrust faults
normal faults
traces of cross-section
mainshocks (M>4.5)
mainshocks (4.0<M<4.5)
aftershocks
N
COLFIORITO
BELLANO
km
a
b
c
x (km)
z (km)

Figure 1

they could not measure any change in the rate of earthquake production.

3. Methodology

[8] We calculate the six components of the stress perturbation ($\Delta\sigma_{ij}$) caused by an earthquake dislocation in a homogeneous half-space using the Okada's formulation [*Okada*, 1985, 1992] and the three-dimensional (3-D) algorithm proposed by *Nostro et al.* [1997]. The Coulomb stress changes are therefore computed using the well-known expression

$$\Delta\mathrm{CFF} = \Delta\tau + \mu(\Delta\sigma_n + \Delta P), \tag{1}$$

where $\Delta\tau$ are the shear stress changes calculated along the slip direction on the assumed fault plane, $\Delta\sigma_n$ are the normal stress changes (positive for extension), μ is the friction coefficient and ΔP indicates the pore pressure changes. Two different models are usually adopted to express the pore pressure changes: the constant apparent friction and the isotropic poroelastic models [see *Beeler et al.*, 2000; *Cocco and Rice*, 2002]. The former is frequently used in Coulomb stress calculations and it is based on the assumption that ΔP is proportional to the normal stress changes

$$\Delta P = -B\Delta\sigma_n, \tag{2}$$

where B is the Skempton coefficient. An alternative, the isotropic poroelastic model assumes that pore pressure changes are proportional to the volumetric (or mean) stress changes (see *Cocco and Rice* [2002] for details):

$$\Delta P = -B\frac{\Delta\sigma_{kk}}{3}. \tag{3}$$

Equation (2) leads to the definition of the apparent friction coefficient $\mu' = \mu(1 - B)$. By substituting (2) in (1) we have the widely used expression to compute Coulomb stress changes [see *Harris*, 1998, and references therein]:

$$\Delta\mathrm{CFF} = \Delta\tau + \mu'\Delta\sigma_n. \tag{4}$$

Equation (3) leads to a different expression of Coulomb stress perturbations: substituting (3) in (1), we obtain

$$\Delta CFF = \Delta\tau + \mu\left(\Delta\sigma_n - B\frac{\Delta\sigma_{kk}}{3}\right). \tag{5}$$

Beeler et al. [2000] pointed out that the two expressions defined in (4) and (5) yield different results; they concluded that the constant apparent friction model defined in (4) may provide a misleading view in estimating stress changes. For these reasons, we will use in this study both relations to compute coseismic Coulomb stress changes.

[9] The expressions discussed above require the calculation of coseismic stress changes caused by an earthquake dislocation for a particular fault plane geometry. In this case, the Coulomb stress perturbations are evaluated directly by resolving the stress perturbation tensor on the adopted fault plane. The calculation of the elastic stress changes on optimally oriented planes for Coulomb failure requires the additional knowledge of the regional stress tensor. *King et al.* [1994] and *King and Cocco* [2001] discuss the details of these calculations. In this case, the fault plane geometry is assumed to be optimally oriented at each node of the 3-D grid. These optimally oriented planes (OOPs) are identified by finding the values of strike, dip and rake angles that maximize the Coulomb stress given by the total stress tensor, defined as

$$\sigma_{ij}^{tot} = \sigma_{ij}^{r} + \Delta\sigma_{ij}, \tag{6}$$

where σ_{ij}^{r} is the regional stress tensor and $\Delta\sigma_{ij}$ is the coseismically induced perturbation. For a given total stress orientation, we find at each node of the 3-D grid two equivalent OOPs (we also refer to these as the conjugate planes for stress), each of which is associated with a particular focal mechanism. The orientations of the OOPs strongly depend on the orientation and magnitude of the regional stress field [*King and Cocco*, 2001; *McCloskey et al.*, 2003]. Therefore the calculations performed through equation (6) allow the computation of Coulomb stress changes at each location on two optimally oriented planes (OOPs), each of which is associated with a focal mechanism derived theoretically.

[10] In the present study, we will first investigate the interaction between the largest-magnitude events of the Umbria-Marche sequence, by computing the Coulomb stress changes onto the assumed rupture planes. In doing these calculations, we will use both expressions of Coulomb stress discussed above (equations (4) and (5)). We will then attempt to model the aftershock pattern, by resolving the Coulomb stress changes either on numerically inferred OOPs or onto the conjugate planes of the focal mechanisms computed from P wave polarity data. In doing these calculations, we use the regional stress orientation inferred for the study area by *Chiaraluce et al.* [2003], who inverted the focal mechanisms of the main events of the 1997 sequence, and we assume a priori the amplitude of a deviatoric stress tensor equal to 2.0 MPa (corresponding to an average value of the static stress drop of the largest earthquakes, see Table 2 and *Pino et al.* [1999]).

4. Stress Changes and Interaction Between Large-magnitude Earthquakes

[11] In this section we present the results of several calculations aimed to model Coulomb stress changes caused by the main shocks of the 1997 Umbria-Marche seismic sequence. We have performed different tests, which are summarized in Table 3, to assess the sensitivity of the

Figure 1. Structural map of the study region [*Collettini et al.*, 2005], showing the major contractional and extensional faults with the Colfiorito 1997 seismicity superimposed [from *Chiaraluce et al.*, 2003]. The traces of the three cross sections and their width are also reported. The gray stars indicate the location of the main events of the sequence. (a, b, and c) Three vertical cross sections showing the distribution of the seismicity with depth.

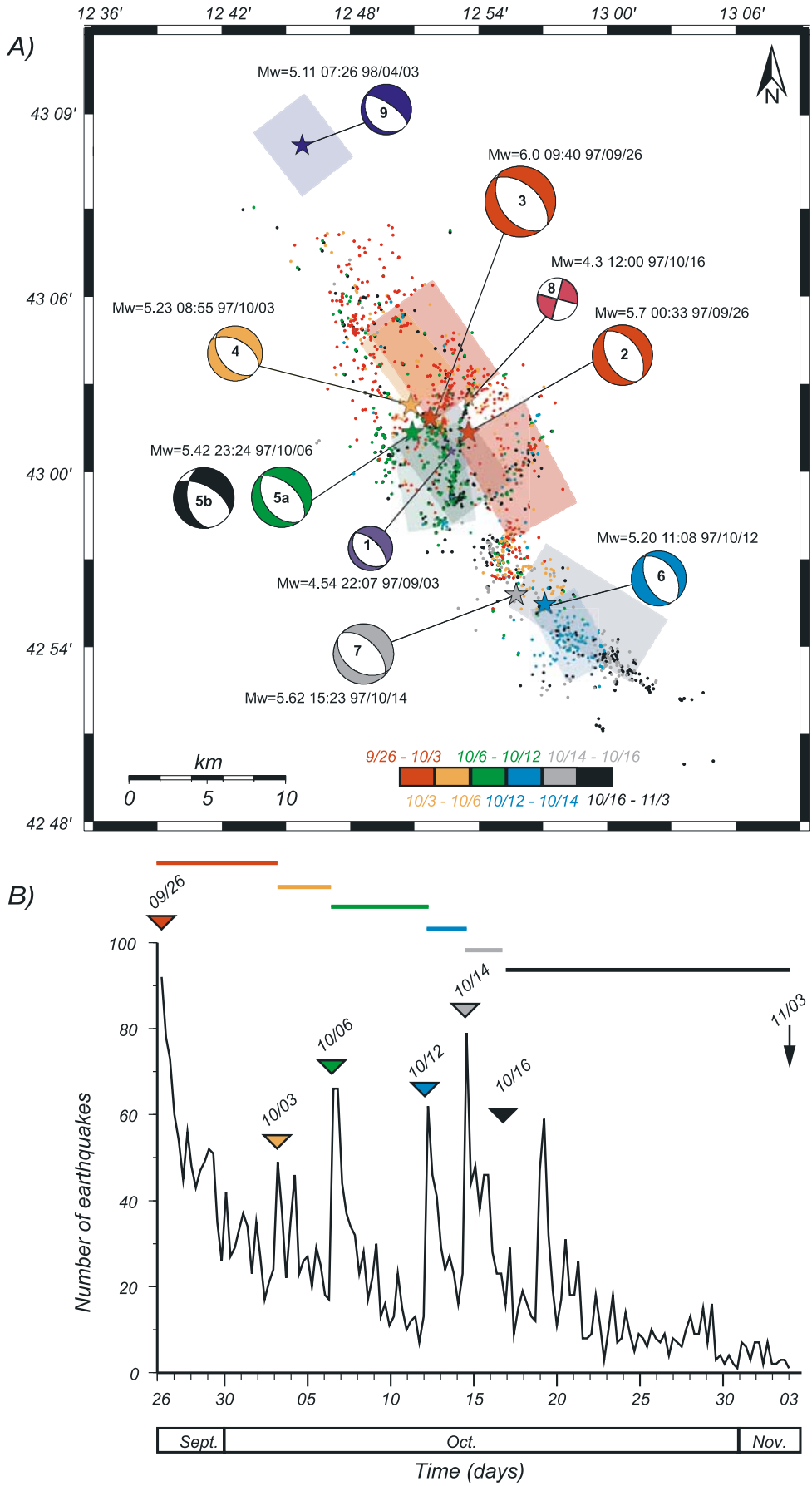
A)
12 36'
12 42'
12 48'
12 54'
13 00'
13 06'
43 09'
43 06'
43 00'
42 54'
42 48'
N
Mw=5.11 07:26 98/04/03
Mw=6.0 09:40 97/09/26
Mw=4.3 12:00 97/10/16
Mw=5.23 08:55 97/10/03
Mw=5.7 00:33 97/09/26
Mw=5.42 23:24 97/10/06
Mw=4.54 22:07 97/09/03
Mw=5.20 11:08 97/10/12
Mw=5.62 15:23 97/10/14
km
0 5 10
9/26 - 10/3 10/6 - 10/12 10/14 - 10/16
10/3 - 10/6 10/12 - 10/14 10/16 - 11/3
B)
09/26
10/03
10/06
10/12
10/14
10/16
11/03
Number of earthquakes
0 20 40 60 80 100
26 30 05 10 15 20 25 30 03
Sept. Oct. Nov.
Time (days)

Figure 2

Table 1. Source Parameters for the Main Shocks[a]

Event	Date	Longitude,[b] °E	Latitude,[b] °N	Length, km	Width, km	Depth,[b] km	M_w[c]	M_0,[c] $10^{16} \times$ N m	Slip, m	Strike,[c] deg	Dip,[c] deg	Rake,[c] deg
1	3 Sept. 1997	12.8787	43.0118	2.5	1.25	4.00	4.54	0.80	0.050	137	30	292
2	26 Sept. 1997	12.8917	43.0225	7.0	7.0	5.70	5.66	40.00	0.27[d]	152	46	277
3	26 Sept. 1997	12.8622	43.0305	12.0	7.0	5.70	5.99	126.00	0.33[d]	142	39	273
4	3 Oct. 1997	12.8475	43.0380	5.0	5.0	4.81	5.2	8.60	0.120	141	43	286
5a	6 Oct. 1997	12.8486	43.0227	6.0	6.0	5.51	5.4	17.00	0.160	145	40	280
5b										170[b]	45[b]	310[b]
6	12 Oct. 1997	12.9518	42.9241	5.0	5.0	4.83	5.2	7.80	0.100	154	51	278
7	14 Oct. 1997	12.9296	42.9292	9.0	6.0	5.97	5.62	34.00	0.27[d]	122	38	260
8	16 Oct. 1997	12.8920	43.0411	1.5	1.5	0.94	4.4	0.39	0.058	18	85	10
9	3 April 1998	12.7617	43.1872	4.8	4.8	6.06	5.1	5.70	0.082	142	30	254

[a]Dates, hypocentral locations [from *Chiaraluce et al.*, 2003], moment magnitude, seismic moment, fault plane solutions [from *Ekström et al.*, 1998], length, width and uniform slip values of the nine main events of the sequence. For event 5 we show two focal mechanism solutions, the first is from *Ekström et al.* [1998], while the second is from *Chiaraluce et al.* [2003].
[b]*Chiaraluce et al.* [2003].
[c]*Ekström et al.* [1998].
[d]For heterogeneous slip, see *Hernandez et al.* [2004].

results to the slip distributions imaged for the three largest events and the two fault plane solutions (CMT and *P* wave polarity mechanisms) available for the 6 October earthquake (shown in Figure 2a). In tests 3 and 4, we have used a uniform slip model on the fault plane scaled to fit the seismic moment (see Table 1). The hypocenters are the same for all tests. We also include in this analysis the 16 October strike-slip event in order to verify if its faulting mechanism is consistent with Coulomb stress transfer. For each of the earthquakes shown in Figure 2a, we compute the Coulomb stress changes caused by the preceding events by resolving the cumulative stress perturbation on the target fault plane. Coulomb stress changes are computed at the earthquake hypocenters projecting the stress changes on both nodal planes of each focal mechanism. We list in Table 4 the Coulomb stress changes also for the auxiliary plane in order to show the computed amplitudes of stress perturbations. Table 4 summarizes the results of our calculations performed by using the apparent constant friction model (equation (4)) for all tests.

[12] Our calculations demonstrate that the best score is obtained for tests 2 and 4, which reveal that only one earthquake (event 4) lies in a negative Coulomb stress area (i.e., stress shadow). In these tests we use different slip distributions (heterogeneous and uniform, respectively) and the same fault plane solutions. We interpret the similarity of the results to mean that the details of the slip distribution may not be that important for the prediction of future impending events, but the precise knowledge of the fault location and geometry is important. We will consider test 2 for the rest of this study, because it uses the most updated information we have. Therefore, for this test we have also computed the Coulomb stress changes using the isotropic poroelastic model (equation (5)) for the whole sequence of nine earthquakes. The results of this further modeling attempt are also listed in Table 4, which confirms the outcomes obtained with the apparent constant friction model.

[13] We show in Figure 3 the results of our calculations for test 2 performed by using the isotropic poroelastic model defined in equation (5). For each event we plot the Coulomb stress changes, calculated by resolving the stress perturbation on the SW dipping plane of the focal mechanism, both in map view at nucleation depth and in cross section. These planes have been selected according to the results of *Chiaraluce et al.* [2003], who identified the rupture planes of the largest earthquakes of the Umbria-Marche sequence by analyzing aftershock distributions. We start our modeling attempts from the foreshock that struck the Colfiorito area on 3 September 1997 (event 1). Figure 3a shows the Coulomb stress changes caused by the foreshock projected onto the fault plane of event 2. Figure 3b shows the induced stress perturbation caused by events 1 and 2 onto the fault plane of event 3. Our calculations point out that hypocenters of both events 2 and 3 are located in areas of positive Coulomb stress and that this result does not depend on the performed test (see Table 4). Figures 3c and 3d present the Coulomb stress changes induced by previous earthquakes on the fault planes of events 4 and 5, respectively. These two earthquakes nucleated a few kilometers away from the two main shocks of 26 September. *Cocco et al.* [2000] failed to explain both these events in terms of Coulomb stress interaction. Our results show that event 4 is the only earthquake modeled in this study that occurred in a stress shadow zone. Figures 3e and 3f display the Coulomb stress changes caused by previous earthquakes onto the fault planes that ruptured during events 6 and 7. These two earthquakes are located in the Sellano area, southeast of the 26 September main shock hypocenters. They are both located in areas of positive Coulomb stress perturbations. Figure 3g shows the Coulomb stress changes caused by the previous seven earthquakes on the fault plane of event 8,

Figure 2. (a) Map view of the seismicity with focal mechanisms [from *Ekström et al.*, 1998] of the main events of the 1997 Umbria-Marche seismic sequence (see Table 1). Rectangles show surface projections of modeled fault segments [from *Chiaraluce et al.*, 2003]. Two focal mechanism solutions for event 5 are reported: 5a (green) is from *Ekström et al.* [1998], while 5b (black) is from *Chiaraluce et al.* [2003]. The epicenters are color coded by time intervals defined by the six main shocks. Numbers in the focal sphere are sequential in time. (b) Plot of the number of earthquakes versus time. The colored triangles indicate the main event occurrences.

Table 2. Principal Axes of the Tectonic Stress

	Amplitude, MPa	Trend, deg	Plunge, deg
σ_1	−2.0	160.77	75.29
σ_2	0.0	−37.96	13.89
σ_S	2.0	53.10	4.55

Trend, plunge and relative amplitude of the principal axes of the stress tensor obtained for the study area by *Chiaraluce et al.* [2003].

which is the M_w 4.3 strike-slip earthquake. Finally, Figure 3h displays the Coulomb stress changes caused by the strongest events of the 1997 sequence on the fault plane of the 1998 Gualdo Tadino earthquake, which is also located in a positive stress area. *Cocco et al.* [2000] did not model events 8 and 9.

[14] The Coulomb stress perturbations caused by previous events on the fault plane that ruptured during the 6 October earthquake are positive only if the focal mechanism inferred by *Chiaraluce et al.* [2003] from *P* wave polarity data is used and only for the nodal plane dipping to the SW (see tests 2 and 4 in Table 4). Therefore we conclude that the modeled Coulomb stress for this event depends on the adopted focal mechanism more than the slip distribution. This explains why *Cocco et al.* [2000], who used the CMT solution for this earthquake, found that this event was located in a stress shadow area. *Chiaraluce et al.* [2003] propose that the 6 October event ruptured a preexisting fault inherited by previous tectonics. We will further discuss this issue. The 3 October earthquake (event 4) is always located in a negative stress area, independently of the main shock slip distributions, in agreement with the results of *Cocco et al.* [2000].

[15] Our modeling results show that seven of the eight earthquakes (i.e., events 2, 3, 5, 6, 7, 8, and 9) modeled in this study initiated in regions of enhanced Coulomb stress. This result persists for all tests; therefore we conclude that static stress interactions between large-magnitude earthquakes do not depend strongly on the adopted slip distributions, even for earthquakes located at relatively close distances (∼3 km). The modeling results obtained for the 16 October 1997 (M_w 4.3, event 8) strike-slip earthquake are very interesting. All the main shocks and most of the aftershocks of the 1997 sequence activated normal faults consistently with the extensional tectonics active in this sector of the Apennines. However, a moderate-magnitude event is located at shallow depth (∼1 km) and it shows a pure left-lateral strike-slip mechanism. Moreover, it was followed by its own sequence of strike-slip aftershocks. The fault plane solution of event 5 inferred from *P* wave polarity data differs from the CMT solution, having a larger component of left-lateral strike-slip motion. These considerations led *Chiaraluce et al.* [2003] to suggest that the N-S shallow structures, inherited by previous tectonics, were reactivated during the 1997 seismic sequence with strike-slip earthquakes. In this paper we show that the left-lateral strike-slip earthquakes may have been promoted by elastic stress interaction. The last event considered in this study occurred in 1998 near the village of Gualdo Tadino, 6 months later and just at the northern edge of the Colfiorito aftershock area. It further extended the seismogenic volume to the northwest along the Apennine direction and it shows a normal faulting mechanism. We will not consider this event in the aftershock analysis because the quality of its aftershock data set is not comparable with that available for the 1997 sequence.

5. Modeling the Aftershock Distribution Through Elastic Stress Changes

[16] In this section we compute the Coulomb stress changes caused by the main shocks of this sequence at the hypocenters of all the well-located aftershocks. We use the isotropic poroelastic model to compute the Coulomb stress changes. Our aftershock catalogue contains 1517 events having formal errors on the order of tens of meters [see *Chiaraluce et al.*, 2003]. In this first attempt to model the aftershock pattern, we consider that the geometry and the faulting mechanisms of the faults where aftershocks nucleated are unknown. Therefore we find the orientation of the optimally oriented fault planes (OOPs) for Coulomb failure. In order to compute the total stress tensor defined in equation (6), we use the orientation and the amplitude of the regional stress tensor listed in Table 2 (see also the inset of Figure 4a). We model the aftershock pattern by evaluating the Coulomb stress changes caused by those main shocks that occurred before the beginning of each of the six time windows drawn in Figure 2b. We consider six time windows, despite the nine main shocks listed in Table 1, because the aftershock catalogue begins after the 26 September 0940 UTM earthquake.

[17] The results of these calculations are summarized in Figure 4. The map of Figure 4a displays the locations of those aftershocks located in areas of positive Coulomb stress (red dots, 82% of the whole data set), while blue symbols indicate those aftershocks located in stress shadow zones. The Figure 4b histogram summarizes the results of Coulomb stress changes at the aftershock hypocenters resolved on the optimally oriented planes for failure (OOPs): for most of the considered time intervals more than 79% of the aftershocks are located in zones characterized by a Coulomb stress increase, with peaks of 90%

Table 3. Different Tests Performed[a]

Test	Slip Model	Fault Plane Solution
1	heterogeneous slip models for events 2, 3, and 7; uniform slip for the others	CMT solutions for all the events
2	heterogeneous slip models for events 2, 3, and 7; uniform slip for the others	*P* wave polarity focal mechanism for event 5; CMT solutions for all the other events
3	uniform slip for all the events	CMT solutions for all the events
4	uniform slip for all the events	*P* wave polarity focal mechanism for event 5; CMT solutions for all the other events

[a]Summary of the four different tests performed to model elastic stress transfer between the largest shocks. See text for explanation. Events for the slip model refer to the events listed in Table 1.

Table 4. Coulomb Stress Changes Caused by the Preceding Events, Computed at the Earthquake Hypocenters Projecting the Stress Changes on Both Nodal Planes of Each Focal Mechanism of the Nine Main Shocks[a]

			CFF on Event, MPa							
Test	CFF Model[b]	Nodal Plane	2	3	4	5	6	7	8	9
1	a	rfp	9.57E-03	1.82E-01	−2.19E+00	−4.24E-02	4.51E-02	1.23E-01	3.39E-01	1.40E-02
1	a	auxiliary	2.49E-02	1.59E-01	−3.00E+00	−8.93E-01	3.87E-02	1.49E-01	3.96E-01	1.49E-02
2	a	rfp	9.57E-03	1.82E-01	−2.19E+00	2.50E-01	4.49E-02	1.18E-01	3.55E-01	1.38E-02
2	a	auxiliary	2.49E-02	1.59E-01	−3.00E+00	−6.99E-01	3.88E-02	1.48E-01	3.47E-01	1.44E-02
3	a	rfp	9.57E-03	1.97E-01	−7.63E-01	−2.66E-02	7.68E-02	1.41E-01	4.72E-01	2.75E-02
3	a	auxiliary	2.49E-02	1.64E-01	−1.01E+00	−6.01E-01	5.78E-02	1.43E-01	3.65E-01	3.44E-02
4	a	rfp	9.57E-03	1.97E-01	−7.63E-01	1.54E-01	7.66E-02	1.37E-01	4.89E-01	2.73E-02
4	a	auxiliary	2.49E-02	1.64E-01	−1.01E+00	−4.73E-01	5.79E-02	1.42E-01	3.16E-01	3.39E-02
2	b	rfp	1.29E-02	2.56E-01	−3.27E-01	1.08E+00	4.11E-02	1.18E-01	3.62E-01	5.43E-03
2	b	auxiliary	4.19E-02	2.14E-01	−1.86E+00	−7.10E-01	2.96E-02	1.74E-01	3.47E-01	6.52E-03

[a]Results of the four different performed test; rfp is the real fault plane. Read 9.57E-03 as 9.57×10^{-3}.
[b]Model a, constant apparent friction model; and model b, isotropic poroelastic model.

during the first time period (26 September to 3 October) and 97% during the second time window. The only exception to this good score is obtained for the time interval comprised between 12 and 14 October, when the two consecutive shocks near Sellano occurred (events 6 and 7, respectively): in this case only 51% of events lie in a positive stress zone. This is evident also in the map of Figure 4a, which shows that the aftershocks for which the induced stress perturbation is negative are mainly located in three areas: on the hanging wall of the fault that ruptured during the 26 September main shocks (event 3), at the southern termination of the N-S inherited structures and in the Sellano area. The total score for the whole sequence of 1517 aftershocks reveal that 82% of them are located in areas of Coulomb stress increase and only 18% lie in stress shadow zones.

[18] These results might be interpreted to support the capability of predicting the aftershock locations in the study area using Coulomb stress transfer. However, we have to point out that for this test Coulomb stress changes have been computed on optimally oriented planes for failure (OOPs), which might differ from the true aftershock fault plane solutions. In order to check this issue, we have therefore resolved the stress perturbation tensor onto the two nodal planes of each aftershock. However, this analysis reduces the aftershock data set to the 322 events for which well constrained focal mechanisms are available. The results of this test are summarized in Figure 5: the two histograms display the number of aftershocks for which the computed Coulomb stress change is positive on both nodal planes (red) or only for one nodal plane (orange) as well as those for which Coulomb stress is negative on both planes (blue). Figure 5 presents the results for both the apparent constant friction model (Figure 5, top) and the isotropic poroelastic model (Figure 5, bottom).

[19] Figure 5 shows that the number of promoted aftershocks (red) is only slightly larger than that occurring in stress shadows (blue), with the exception of the first temporal window in which the number of aftershocks with negative stress changes on both the conjugate planes (blue) is larger than that promoted by Coulomb stress changes (red). If we consider the aftershocks having positive stress changes only for one conjugate plane and negative for the auxiliary (orange in Figure 5) as successes (i.e., triggered events), then for the isotropic poroelastic model the success rate changes from 60% to 73% of the seismic events that are promoted by Coulomb stress perturbations. However, this is a reasonable assumption only if the plane on which the positive stress perturbation is resolved coincides with the rupture plane, which should be verified. We will explore this issue in section 6. Another interesting feature emerging for Figure 5 concerns the number of promoted aftershocks during the first time window (26 September to 3 October): while the number of aftershocks located in areas of positive stress changes for optimally oriented planes for Coulomb failure (OOPs) is very high (90%), it drops to 29% (61% including the orange solutions as successes) when resolving the stress changes onto the conjugate planes of the best constrained fault plane solutions.

[20] In Figure 6 we show the results of the same test in a more accurate way: for each time interval we show two rose diagrams displaying the two sets of OOPs (top semicircle) calculated in this study (each one corresponding to a conjugate plane for stress), the fault plane solutions inferred from data (bottom semicircle) and the radial distribution of the main structural units derived from geological observations (gray lines). For the OOPs, the selected azimuth corresponds to that of the conjugate plane for stress. For the focal mechanism the azimuth is that of the nodal plane

Figure 3. Maps and cross sections of Coulomb stress for each of the Colfiorito main earthquakes (see Table 1). ΔCFF are calculated by resolving the stress perturbation onto the rupture plane of its subsequent earthquake. Maps have been drawn at nucleation depth for each main event. The black focal mechanisms are related to the perturbing events, while the red (ΔCFF positive on both the planes), green (ΔCFF positive only on one plane identified by the thicker line), and blue (ΔCFF negative on both the planes) are related to the target event. (a) Coulomb stress changes caused by the foreshock projected onto the fault plane of event 2. (b) ΔCFF due to events 1 and 2 onto the fault plane of event 3. (c) ΔCFF due to events 1, 2, and 3 onto the fault plane of event 4. (d) ΔCFF due to events 1–4 onto the fault plane of event 5. (e) ΔCFF due to events 1–5 onto the fault plane of event 6. (f) ΔCFF due to events 1–6 onto the fault plane of event 7. (g) ΔCFF due to events 1–7 onto the fault plane of event 8. (h) ΔCFF due to events 1–8 onto the fault plane of event 9.

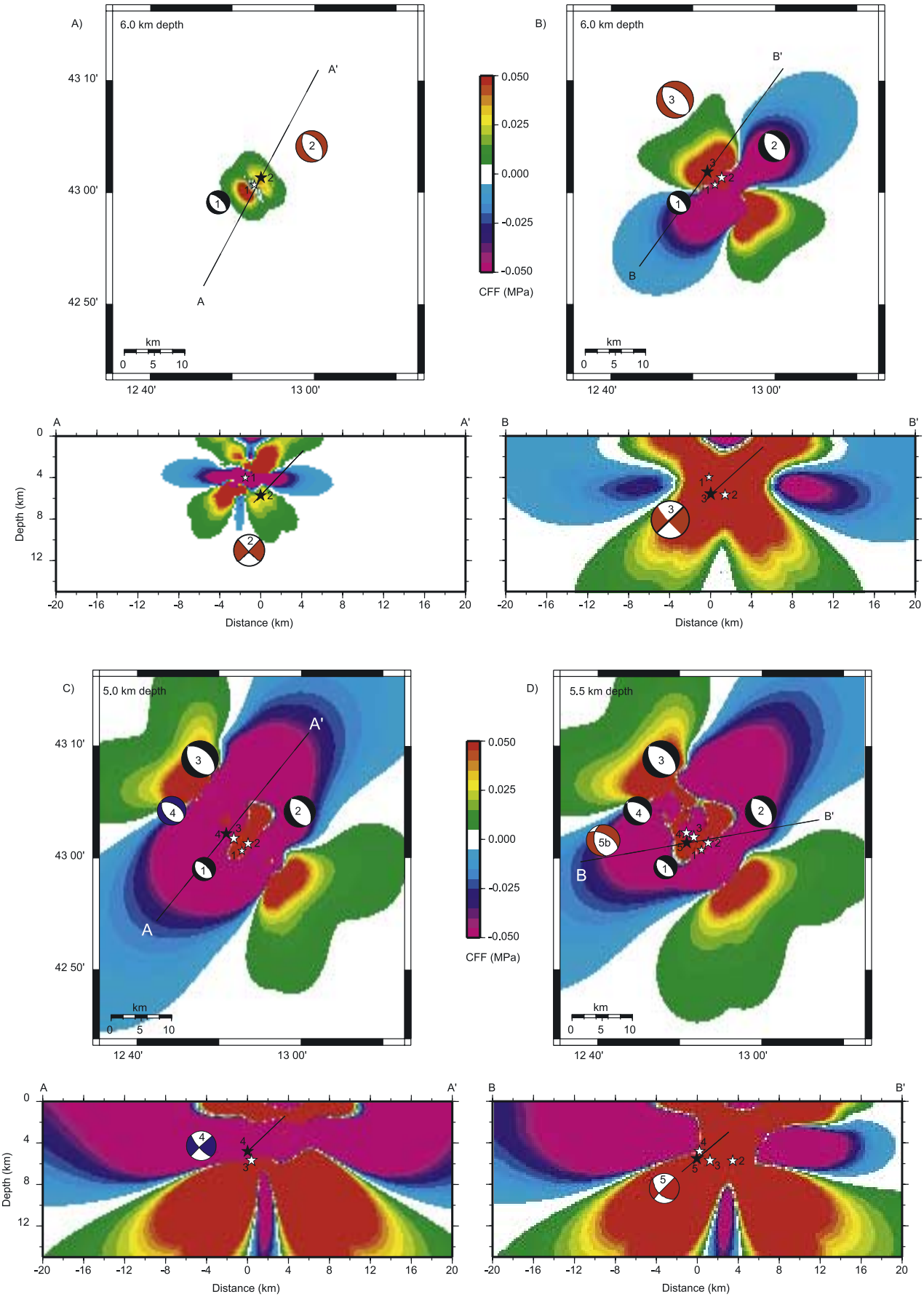
A)
6.0 km depth
A'
A
43 10'
43 00'
42 50'
12 40'
13 00'
km
0 5 10
B)
6.0 km depth
B'
B
0.050
0.025
0.000
-0.025
-0.050
CFF (MPa)
A
A'
B
B'
Depth (km)
Distance (km)
C)
5.0 km depth
D)
5.5 km depth
5b

Figure 3

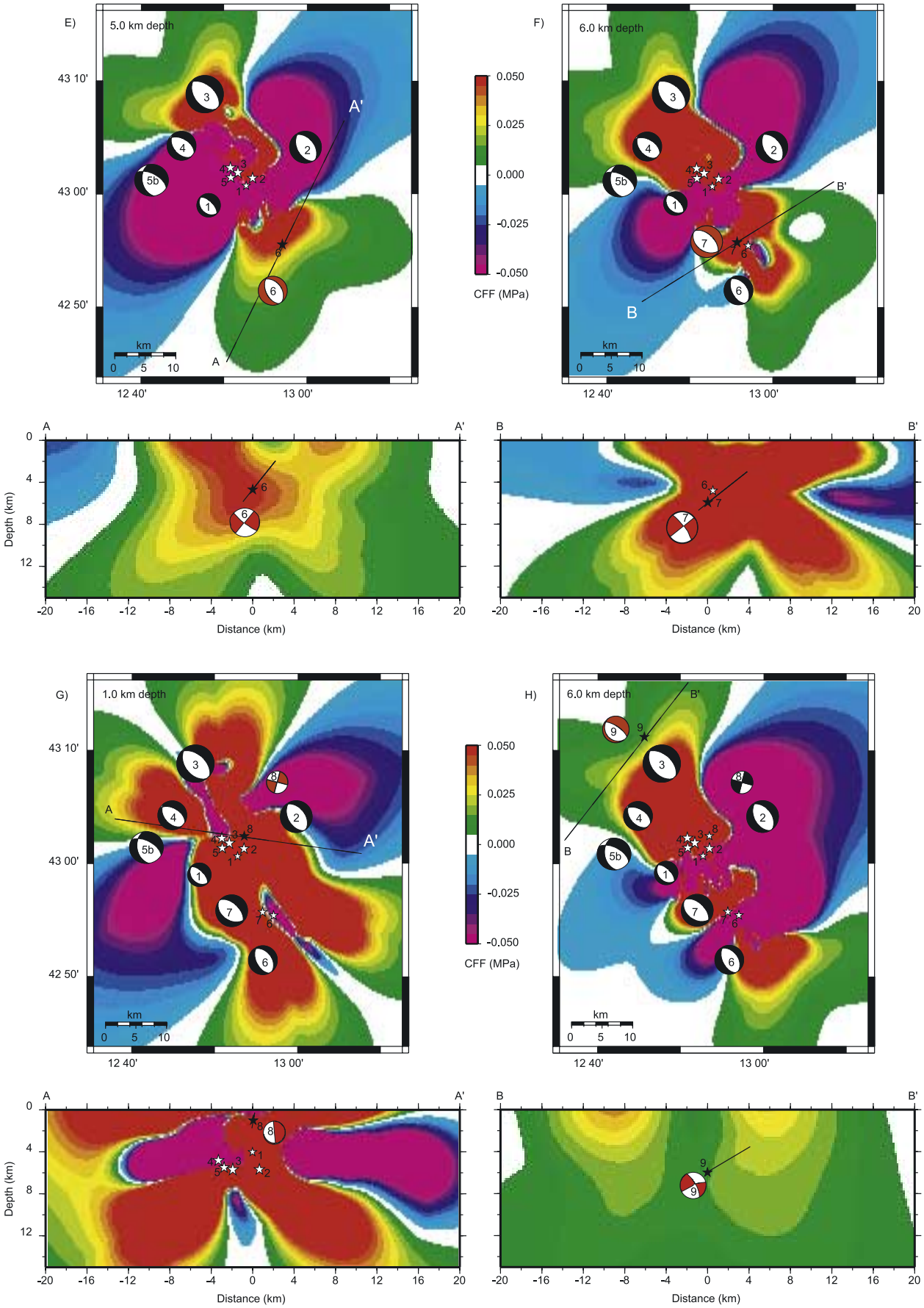

Figure 3. (continued)

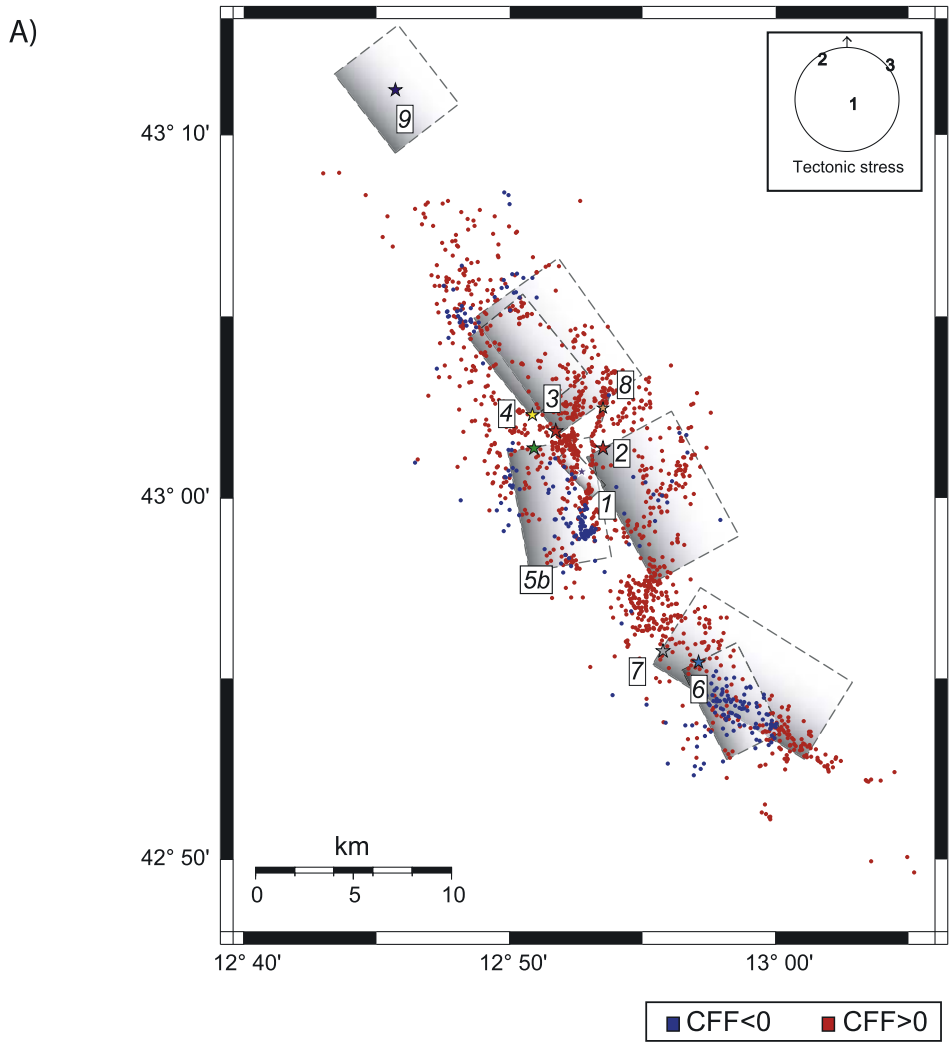

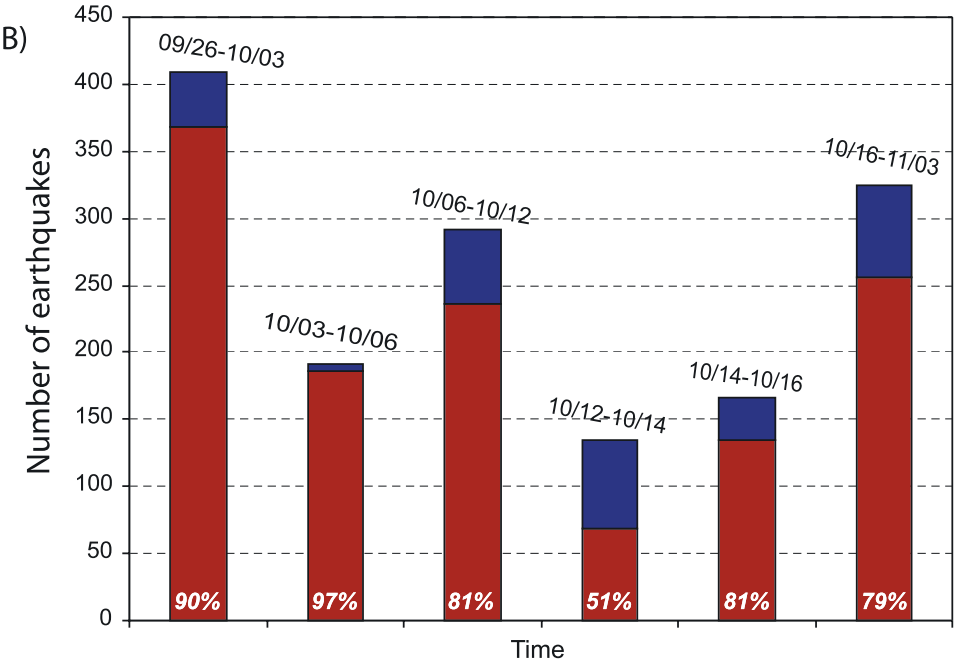

Figure 4. (a) Map of aftershocks located in areas of positive (red dots) or negative (blue dots) Coulomb stress. (b) Histogram summarizing the results of Coulomb stress changes at the aftershock hypocenters resolved on the optimally oriented planes for failure (OOPs) for all the considered time intervals.

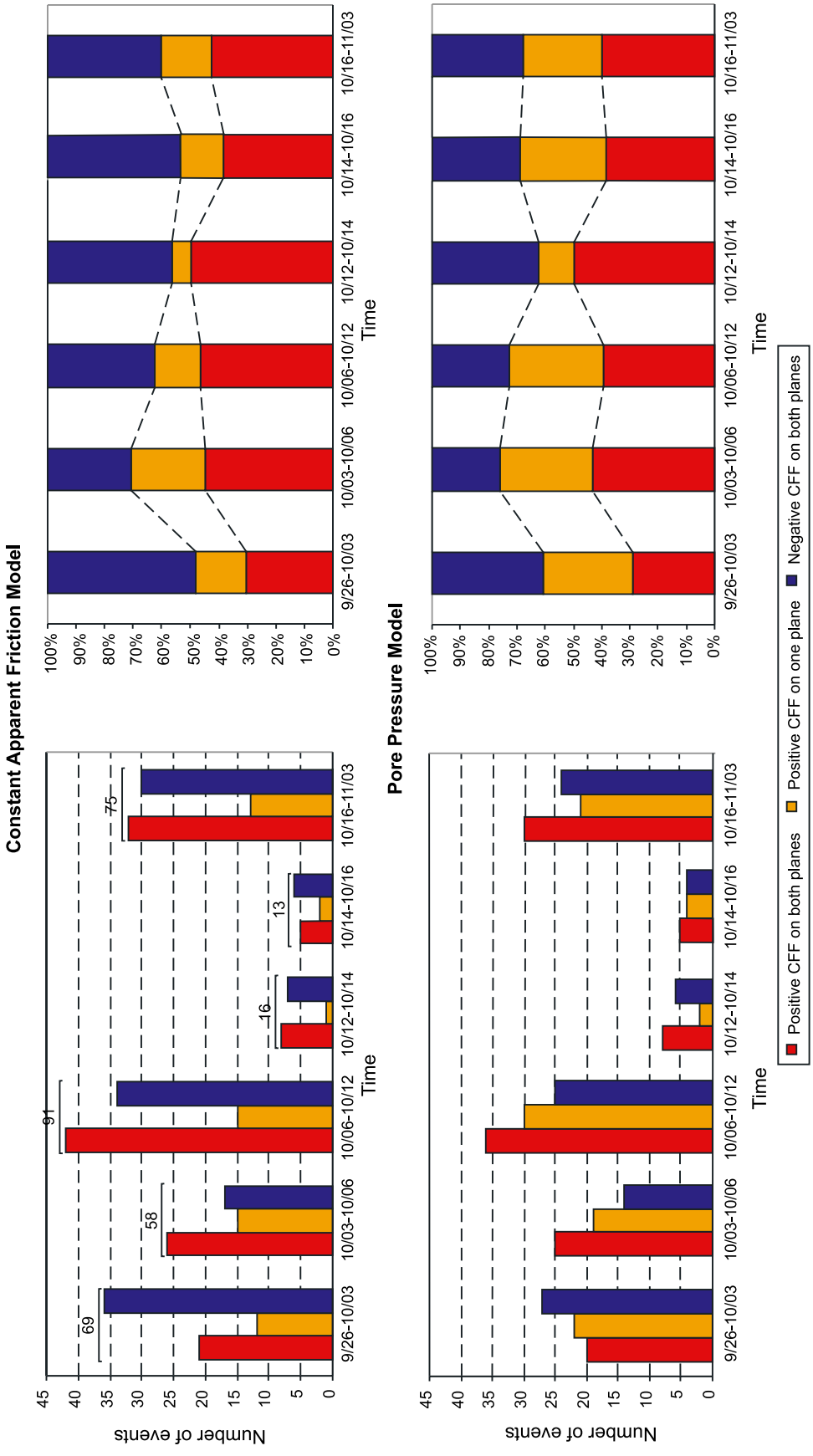

Figure 5. Histogram summarizing the results of Coulomb interactions by resolving Coulomb stress tensor onto the two nodal planes of each aftershocks real focal mechanisms for all the considered time intervals. Results obtained with the (top) constant apparent friction model and (bottom) pore pressure formulations. Red indicates positive ΔCFF on both the planes of the focal mechanism, orange is positive only in one plane, and blue is negative on both the planes.

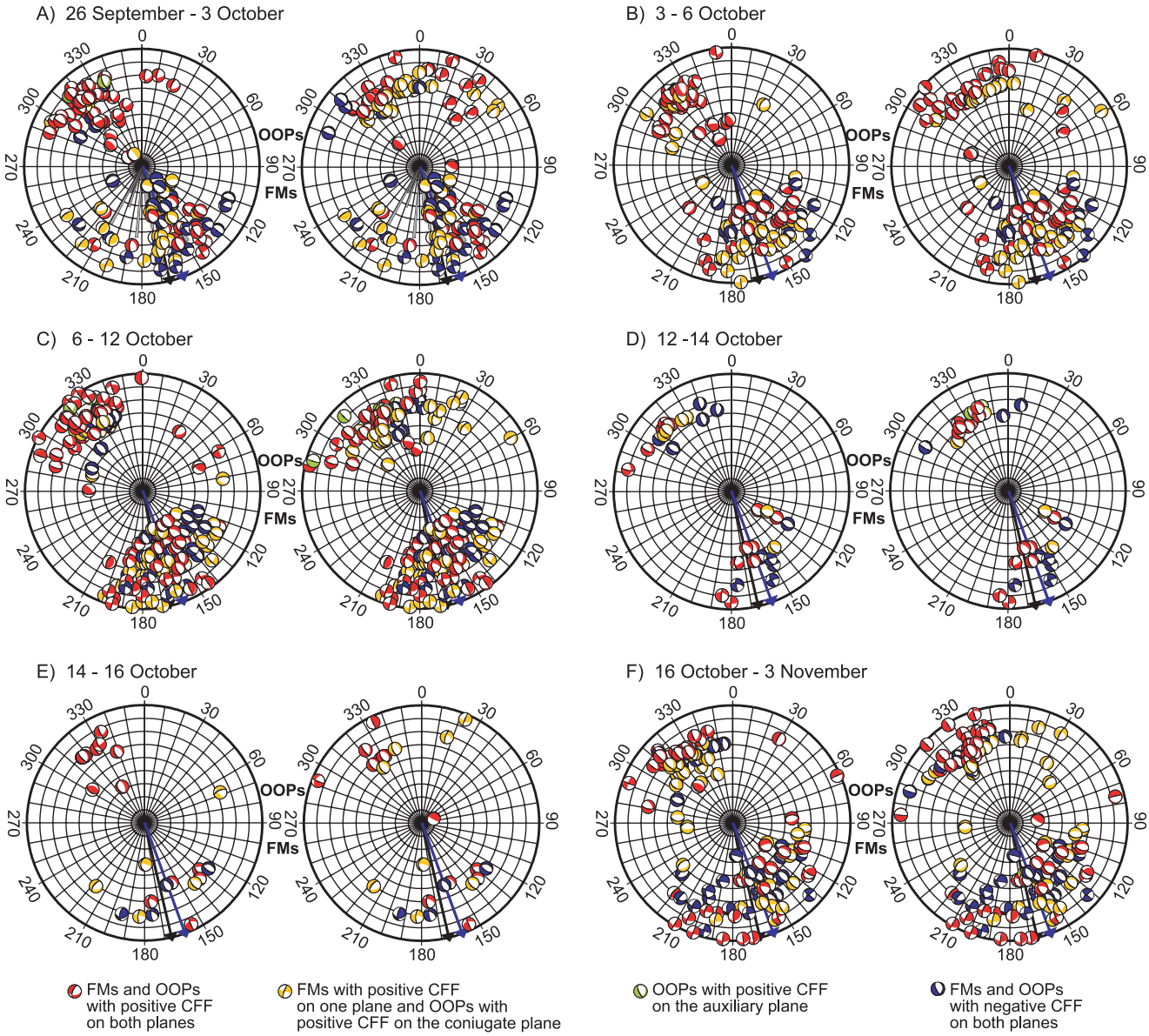

Figure 6. Rose diagrams computed for each time interval display in the top semicircle the OOPs computed in every point of the volume where we have focal mechanism solutions available. The corresponding fault plane solutions computed with the first motion polarity data [from *Chiaraluce et al.*, 2004] are displayed in the bottom semicircle. Red mechanisms indicate those aftershocks for which the Coulomb stress changes are positive on both the nodal planes; the orange mechanisms identify those aftershocks for which the Coulomb stress is positive only for one plane (corresponding to the conjugate plane for stress) and negative for the other; green mechanisms identify those aftershocks for which the Coulomb stress is negative on the conjugate plane for stress but positive on the auxiliary plane. The blue mechanisms indicate those aftershocks for which stress perturbation is negative on both planes. Coulomb stress changes for this test have been computed using the isotropic poroelastic model. Gray lines show the radial distribution, scaled with the length, of the faults of the area derived from the geological map illustrated in Figure 1. The black arrow defines the average orientation of the whole set of mapped geological faults, while the blue arrow identifies the average strike orientation resulting from focal mechanisms computed from polarity data.

closest to the orientation of the fault segment identified by seismological observations, equivalent to choosing the orientation of the plane which has experienced the greatest stress increase. Coulomb stress changes for this test are computed using the isotropic poroelastic model, which gives the best score (see Figure 5). The black arrow defines the average orientation of the whole set of mapped geological faults (shown in Figure 1), while the blue arrow identifies the average strike orientation resulting from focal mechanisms. The length of the radial segments indicating the orientations of geological structures scales with the number of observed fault's strikes. Each diagram pair associated with a particular time interval displays the same true fault plane solutions (bottom semicircle).

[21] Figure 6 emphasizes several important results: (1) the number of events for which Coulomb stress is negative on both planes is greater when focal mechanism planes are assumed instead of the OOPs (Figures 4b and 5); (2) the pattern of fault orientations inferred from the aftershock's focal mechanisms is very similar to those retrieved from mapped geological faults (in other words they spread over the same range of azimuths); (3) OOPs do not contain low-angle dipping normal faults (see Figures 6a and 6b), while fault plane solutions show many of them (focal mechanisms are closer to the center of the circle); (4) some OOPs show reverse movement which is not seen in the data (see Figure 6b); and (5) in the time period shown in Figure 6c OOPs and focal mechanisms have a similar mixture of strike-slip and normal faulting events, while in Figure 6f the majority of focal mechanisms are strike slip, and OOPs are mainly normal events. There is another relevant result emerging from Figure 6: for most of the solutions (90%) with one positive and one negative stress change (orange symbols) the nodal plane for which the stress change is positive (marked in bold in each mechanism) coincides fairly well with the average orientations of the mapped geological faults. For normal faulting aftershocks this nodal plane corresponds to the SW dipping faults that have been activated during the sequence (see *Chiaraluce et al.* [2003] for further details). For strike-slip aftershocks the nodal plane with positive stress change is consistent with the orientation of the nearly N-S shallow structures inherited from previous tectonics (see *Collettini et al.* [2005] for further details). These results suggest that there is a structural control on aftershocks promoted by Coulomb stress perturbations and cause us to speculate that the orange solutions might be included in the final score of triggered seismicity and considered as successes.

[22] These interpretations motivate two further tests. We compute the Coulomb stress changes on OOPs having the strike constrained by the average orientations inferred from geological mapped faults and then we compare these to the focal mechanisms inferred from *P* wave polarity data. We will discuss the results of these tests in the next section.

6. Computing Coulomb Stress Changes Using Constraints From Structural Geology

[23] We compute the Coulomb stress changes caused by the preceding main shocks at the hypocenters of the 322 aftershocks considered above and we resolve the stress changes onto OOPs having the strike of the target faults fixed a priori. We use the information from structural geology (see Figure 1) to impose the strike of the OOPs. In other words, we compute the stress changes on OOPs having a predetermined strike orientation, while dip and rake angles are those that maximize the Coulomb failure function. We define several structural constraints: a strike orientation identified as the average strike of the whole fault population shown in Figure 1 (corresponding to N167°); the same orientation but allowing for a variation defined as the standard deviation (N167° ± 23°); the average strike orientation calculated only for normal faults (N145° ± 8°) or only for thrust faults (N175° ± 13°), respectively.

[24] The results of these calculations are summarized in Figure 7 (the adopted color code is the same used in Figure 6). Figure 7 reveals that computing stress changes onto OOPs with predetermined strike orientations does not improve the results found for the OOPs without any constraints (second and third columns in Figure 7). In particular, the number of events having a positive stress changes on both the nodal planes (red) decreases (as in the first time window) or remains nearly the same of unconstrained OOPs (OOPs1 and OOPs2 in Figure 7). The percentage of aftershocks having a positive stress change for one nodal plane (coinciding with the conjugate plane for stress) and negative for the other (orange) varies depending on the imposed structural constraint. Moreover, Figure 7 again emphasizes the clear difference between the score resulting from resolving stress changes onto the fault plane solutions inferred from data (first column in each panel) and that resulting from OOPs, even with structural constraints.

[25] We have therefore compared the predicted focal mechanisms (those resulting from OOPs) with the fault plane solutions inferred from data. We show the result of this comparison in Figure 8. We perform the comparison between focal mechanisms in the following way: we consider similar those fault plane solutions having a difference smaller than 20°, 30°, 45° in strike, dip and rake angle, respectively, which corresponds to two times the formal errors in computing focal mechanisms [*Chiaraluce et al.*, 2004]. We discard all the solutions that do not lie within these intervals. It is important to point out that the number of fault plane solutions is not uniformly distributed within the different time windows: in particular the number of focal mechanisms for aftershocks occurred within the two time windows between 12–14 and 14–16 October is much smaller than those in the other windows. Figure 8 shows that the adoption of geological constraints does not improve the capability to predict the fault plane solutions: the OOPs calculated without constraints better agrees with the true focal mechanisms. Moreover, the number of aftershocks whose predicted focal mechanism is similar to that computed from observations is very small. Within the first time window only 32% of the predicted fault plane solutions agree with the true ones. In the first three time windows, where we have a good data set of focal mechanisms, the agreement between predicted and observed solutions never exceeds 45%. A slightly better score is found for the last window where we found that 50% of the predicted and observed mechanisms are in agreement. If we restrict the analysis to the largest-magnitude aftershocks ($M > 3.4$) the score slightly improves in the first three time windows (we remind here that we did not consider in this analysis the

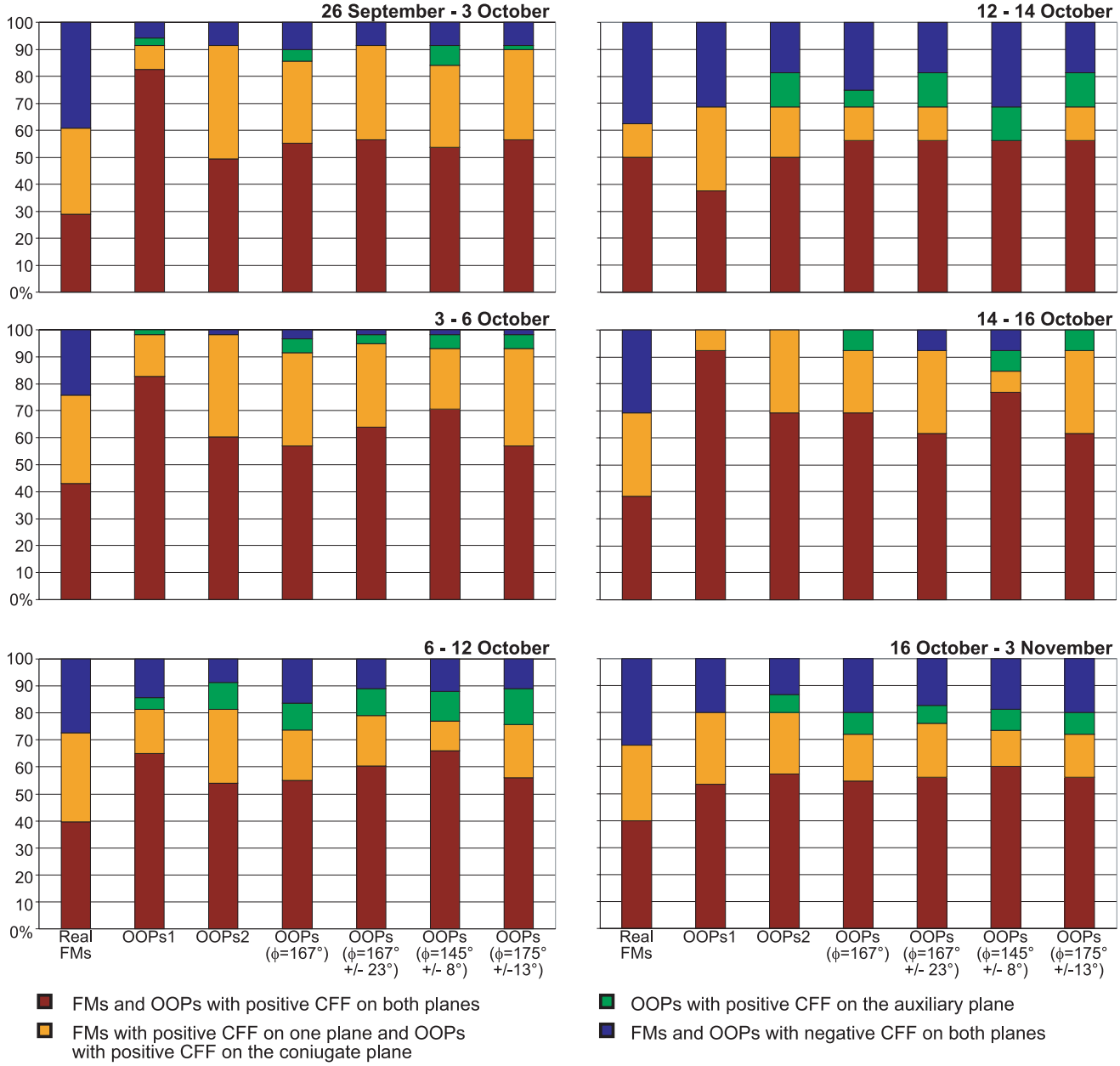

Figure 7. Histograms for each time interval show results obtained by using different constraints derived from the structural geology information. Red and blue indicate the aftershocks for which the Coulomb stress changes are positive or negative on both the conjugate planes. Orange indicates those aftershocks for which the Coulomb stress is positive on only one conjugate plane, which coincides with the plane where the CFF is maximum. Green indicates those aftershocks for which the Coulomb stress is negative on the conjugate plane where the CFF is maximum, but it is positive on the auxiliary ones.

main shocks listed in Table 1): 50% to 60% of the predicted focal mechanisms agree with the observed ones. Therefore we conclude that the capability to predict fault plane solutions with optimally oriented planes for Coulomb failure in the study area is modest.

7. Reactivation of Preexisting Faults Inherited by Previous Tectonics

[26] *Chiaraluce et al.* [2003] have shown that most of the aftershocks of the 1997 sequence (70%) are consistent with a uniform NE trending extensional stress field and show dominant normal faulting. Another fraction (25%) of aftershock focal mechanisms that cannot be explained by an extensional stress field are related to the pattern of shallow strike-slip events. These events occurred on faults that have been interpreted by *Chiaraluce et al.* [2003, 2004] as a possible reactivation of a portion of an inherited lateral thrust ramp with seismicity characterized by left-lateral faulting. The main shock of 16 October 1997 (M_w 4.3) is the largest earthquake located on this shallow N-S trending fault and it is characterized by a left-lateral strike-slip

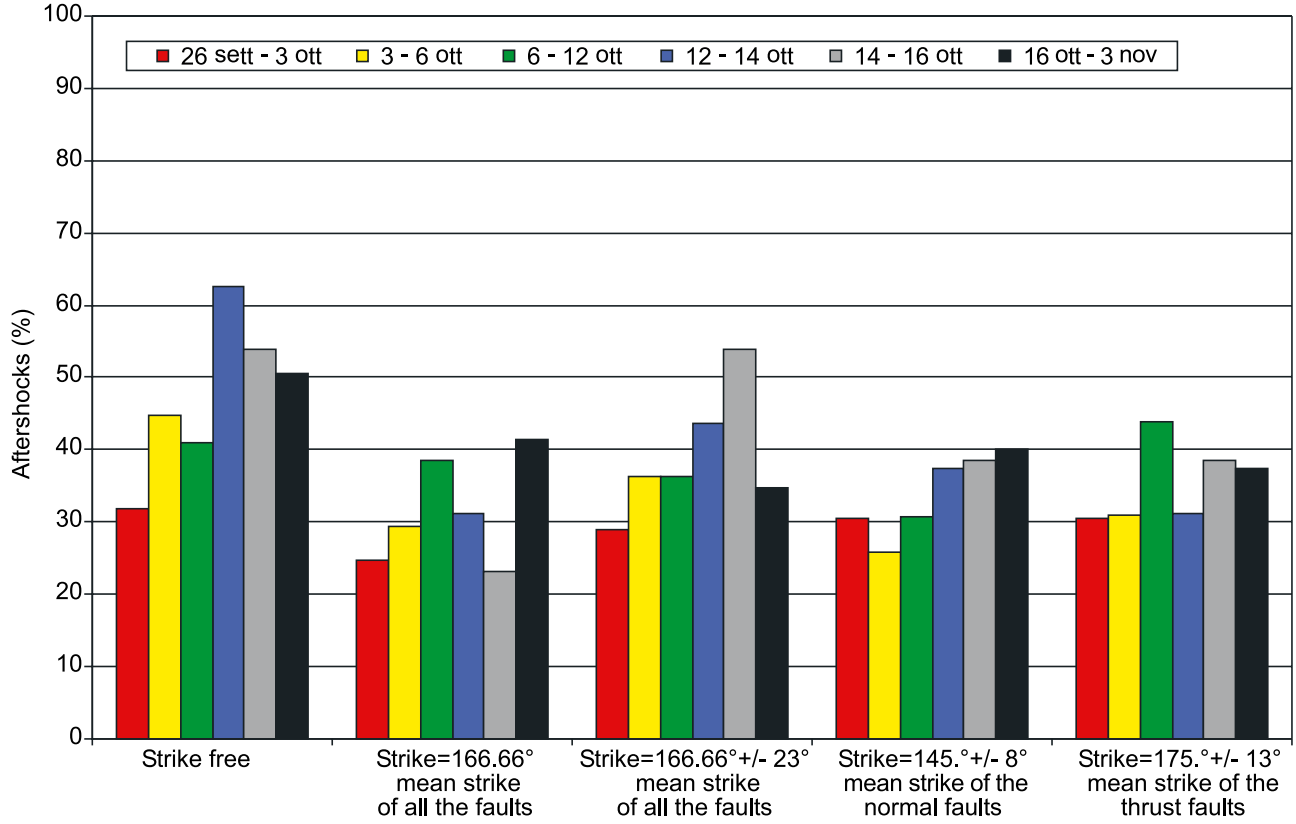

Figure 8. Histograms showing the comparison between the OOPs obtained by using different structural constraints (see text for explanation) with the focal mechanisms solutions for each time interval.

mechanism (see Figure 2a and Table 1). We have already shown in Figure 3 that the 16 October earthquake is located in an area of positive Coulomb stress changes caused by the previous main shocks. In this section we analyze the Coulomb stress changes caused by the normal faulting main shocks of the sequence and resolve them onto the fault planes of all the N-S striking aftershocks in order to test if the strike-slip aftershocks are promoted by elastic stress changes. Many strike-slip events occurred immediately after the 26 September (event 3) and after the 6 October main shock (see Figure 2). This means that the shallow N-S trending strike-slip fault was active also before the occurrence of the 16 October event. For this reason we analyzed separately the strike-slip events that occurred before and after the 16 October 1997 event.

[27] The results of our modeling indicate that 36 out of 87 strike-slip aftershocks (41%) that occurred before the 16 October earthquake have positive Coulomb stress changes on both the nodal planes and 33% have positive stress perturbations for one nodal plane and negative for the other. Moreover, 53% of the strike-slip aftershocks that followed the 16 October event earthquake have positive Coulomb stress changes on both the nodal planes and 17% have positive stress perturbations only on one nodal plane (red and orange symbols in Figure 9b, respectively). It is important to note that for strike-slip aftershocks the nodal plane with maximum and positive stress change (marked in bold in Figure 9) coincides with the orientation of the nearly N-S shallow structures identified by geological observations and associated with faults inherited from previous tectonics. Thus, in this case we believe that these strike-slip aftershocks for which Coulomb stress is positive only for one nodal plane (orange mechanisms) can be considered as events promoted by Coulomb stress changes.

[28] The performed analysis clearly shows that the normal faulting earthquakes have promoted the strike-slip events on the N-S shallow structures increasing the Coulomb stress both at the hypocenter of the shallow strike-slip main shock and on large portions of the N-S inherited structures. These modeling results also explain why seismicity activated this N-S fault system immediately after the two main shocks of 26 September. It is important to emphasize that the N-S fault system is mapped by field geologists (see Figure 1) as a right-lateral fault created during the past compressive tectonic phase [see *Collettini et al.*, 2005, and references therein]. Therefore the stress redistribution due to the sequence of normal faulting earthquakes not only reactivated this fault system inherited by previous tectonics but also inverted the slip.

8. Discussion and Conclusion

[29] The main goal of this study is the investigation of fault interaction through elastic stress transfer among the subsequent moderate size earthquakes that occurred during the 1997 seismic sequence in the central Apennines. We also investigate the spatial pattern of aftershocks and we try to explain it in terms of Coulomb stress changes caused by sequences of subsequent main shocks. To this goal we compare the focal mechanisms inferred from *P* wave

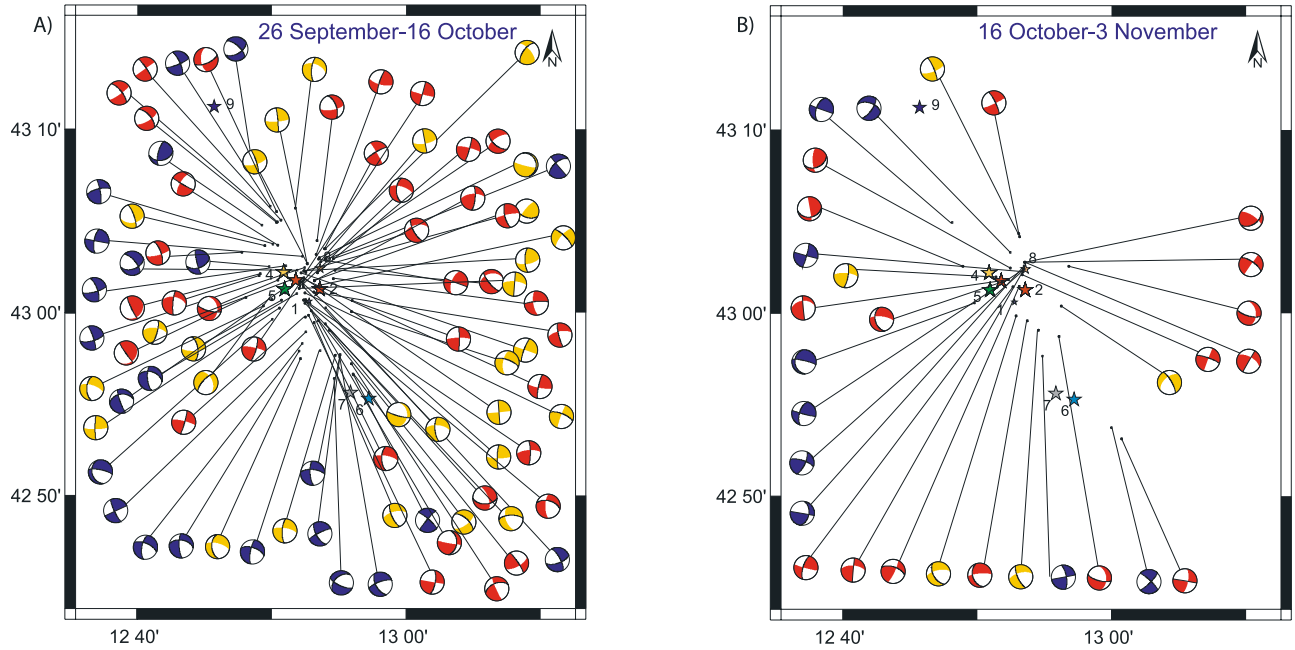

Figure 9. ΔCFF computed on the strike-slip focal mechanisms solutions for the aftershocks occurred (a) before and (b) after the 16 October earthquake (event 8). Red indicates the solutions with positive Coulomb stress changes in both the planes, orange indicates only in one plane, while blue is used for the solutions negative for both planes.

polarity data with those predicted for optimally oriented planes (OOPs) for Coulomb failure. The availability of new and original results on the source process of the three main events [*Hernandez et al.*, 2004], the complex pattern of fractures and fault systems [*Chiaraluce et al.*, 2003; *Collettini et al.*, 2005, and references therein] as well as aftershock locations and fault geometry [*Chiaraluce et al.*, 2003, 2004] motivated this study.

[30] We confirm the results of *Cocco et al.* [2000] and extend them, showing that seven out of eight main events are located in areas of positive Coulomb stress changes. We note that for the 6 October main shock the sign of the induced stress changes depends on the assumed focal mechanism: if the CMT solution, consisting in a pure normal faulting, is adopted (as done by *Cocco et al.* [2000]) this event lies in a stress shadow zone. On the contrary, if the focal mechanism resulting from *P* wave polarities [see *Chiaraluce et al.*, 2003] is used to compute the induced stress perturbations, this event lies in an area of enhanced Coulomb stress. This latter mechanism is consistent with aftershock distribution and with the local tectonic setting. *Chiaraluce et al.* [2003] have shown that inherited compressional structures control the segmentation of the NW trending Quaternary active normal faults. Our modeling results show that the activation of the N-S structures has been promoted by elastic coseismic stress changes caused by the normal faulting earthquakes. The adoption of an isotropic poroelastic model to compute the Coulomb stress perturbations [*Cocco and Rice*, 2002] yields a better correlation between positive stress changes and the location of main shocks of the 1997 seismic sequence.

[31] The only main shock that always lies within a stress shadow zone is the 3 October earthquake. This event is located in the hanging wall or on the same fault plane that ruptured during the 26 September main shock. In this latter case, it is important to point out that it nucleated within a high slip patch of the 26 September shock [*Hernandez et al.*, 2004]. A candidate mechanism to explain the repeated dislocation of the same fault portion during two distinct events is the fluid pressurization of the fault zone [*Segall and Rice*, 1995]: the increase of pore pressure driven by the previous dislocation can contribute to reload the fault patch. *Miller et al.* [2004] suggest that seismicity on the hanging wall of the main faults can be driven by a pressure pulse originated coseismically from a deep source of trapped high-pressure fluids propagating into the damage region created at the time of the earthquake. Both these interpretations can explain the occurrence of the 3 October earthquake in the stress shadow zone caused by previous main shocks.

[32] The modeling results presented in this study allow us to conclude that elastic stress transfer promoted the occurrence of the largest-magnitude earthquakes of the Umbria-Marche seismic sequence. *Steacy et al.* [2004] have shown that fault models incorporating the correct rupture geometry but greatly simplified slip distributions produce stress fields consistent with the aftershock pattern when the near-source events are excluded. Our results agree with these conclusions: we have shown that the slip distribution is not so relevant to model Coulomb stress perturbations and fault interaction among the largest-magnitude events of the Umbria-Marche sequence. The interevent distance between main shocks ranges between 3 and 10 km, if we exclude the 3 October earthquake, and it is smaller than the average size of the main fault planes. However, we have to remark that the variable slip models proposed by *Hernandez et al.* [2004] and used in our stress modeling are relatively smooth. It might be possible that actual slip distributions can be more heterogeneous at short wavelengths, and this

might explain the difficulties in predicting the focal mechanisms of aftershocks located at close (<3 km) distances from the fault planes.

[33] The aftershock pattern characterizing the 1997 Umbria-Marche seismic sequence shows a peculiar spatial and temporal evolution (see Figure 2). Our modeling results indicate that most (82% out of 1517) of the aftershocks are located in areas of enhanced Coulomb stress (see Figure 4). Therefore we might conclude that the spatial distribution of aftershocks is consistent with Coulomb stress changes, with seismicity primarily occurring in areas experiencing positive stress changes. However, our analyses demonstrated that the number of promoted aftershocks decreases when stress changes are resolved onto the nodal planes of focal mechanisms computed from polarity data (see Figure 5); moreover, most of these positive stress changes are calculated on optimally oriented planes (OOPs) that differ from the computed focal mechanisms (see Figure 8).

[34] *McCloskey et al.* [2003] suggest that the common practice of resolving stress changes onto optimally oriented planes for Coulomb failure is not supported by observations and propose that aftershock failure planes are controlled by geological structures. We have tested this issue in our study by calculating different sets of OOPs having the strike angle fixed a priori by geological observations. Our results suggest that despite the agreement between the average orientation of aftershock rupture planes and the orientation of the geological structures mapped at the surface (see Figures 1 and 6), the structural constraints do not improve the agreement between OOPs and observed fault plane solutions (see Figure 8). Nevertheless, it is worth noting that, for those aftershocks having a positive stress change for one nodal plane (coinciding with one of the two conjugate planes for stress) and negative for the other (indicated in orange in Figure 8), the conjugate plane of the focal mechanism with the maximum Coulomb stress increase is often consistent with the average strike orientation of mapped faults. This suggests that a structural control does exist. Thus we can conclude that the join prediction of both location and focal mechanism of an impending aftershock remains an extremely difficult task in the study area. It is important to note that most of the analyses of earthquake triggering relying on the correlation between seismicity rate changes and Coulomb stress perturbations do not account for the faulting mechanisms of promoted aftershocks. This approach has the advantage to provide a robust statistical measure of the increase in the rate of earthquake production in a seismogenic area. However, it contains the same limitations we have experienced in our application to the 1997 Umbria-Marche seismic sequence.

[35] Performing an accurate statistical test of aftershock triggering is beyond the goals of this study. This issue was already examined by several authors [*Hardebeck et al.*, 1998; *Anderson and Johnson*, 1999; *Seeber and Armbruster*, 2000]. *Kilb et al.* [1997] investigated the origin of diverse aftershock mechanisms following the 1989 Loma Prieta earthquake and concluded that the inability to duplicate aftershock mechanisms reliably might be due to the combined uncertainties in models of main shock slip distribution, background stress field and aftershock locations. On the other hand, the Umbria-Marche seismic sequence is characterized by the similarity of fault plane solutions of main shocks and aftershocks: 70% of the events show normal faulting solutions and 24% show left-lateral strike-slip mechanisms. The latter are located on well-identified N-S shallow structures inherited from previous tectonics. Nonetheless, our modeling results confirm the findings of *Kilb et al.* [1997] concerning the incapability to reliably reproduce aftershock mechanisms. This might be due in our opinion to (1) the complex fault mesh and to the 3-D tectonic setting characterizing such a relatively small seismogenic volume; (2) the poor knowledge of the absolute stress amplitudes and the depth dependence of the tectonic stress tensor; (3) the details of slip distributions at short wavelength that can affect the prediction of focal mechanisms for aftershocks located very close to the main rupture planes; and (4) the presence of fluids and the pore pressure relaxation caused by coseismic (undrained) stress changes. *Antonioli et al.* [2005] have shown that the spatial and temporal migration of seismicity is consistent with the pore pressure relaxation caused by elastic stress changes in a fluid-saturated poroelastic medium. They modeled the temporal migration of seismicity in terms of pore pressure relaxation governed by the Darcy law and estimated a hydraulic diffusivity value ($\sim$50 m^2/s) consistent with observations in other areas. The presence of low-angle dipping normal faults (see Figures 6a and 6b) in fault plane solutions, in a tectonic setting with a nearly vertical σ_1, corroborates the hypothesis of the presence of fluid at nucleation depth. The results of our study support the idea that both elastic and poroelastic effects control the seismicity pattern during the Umbria-Marche sequence.

[36] **Acknowledgments.** We thank Claudio Chiarabba, Alessandro Amato, Massimiliano Barchi, and Cristiano Collettini for the useful discussions. This research began in the framework of the EC project PRESAP. We thank the project participants, in particular, John McCloskey and Sandy Steacy for the scientific discussions. We thank Joan Gomberg and Geoffrey King for the helpful revision of this paper.

References

Amato, A., et al. (1998), The 1997 Umbria-Marche, Italy, earthquake sequence: A first look at the main shocks and aftershocks, *Geophys. Res. Lett.*, *25*, 2861–2864.

Anderson, G., and H. Johnson (1999), A new statistical test for static stress triggering: Application to the 1987 Superstition Hills earthquake sequence, *J. Geophys. Res.*, *104*, 20,153–20,168.

Antonioli, A., D. Piccinini, L. Chiaraluce, and M. Cocco (2005), Fluid flow and seismicity pattern: Evidence from the 1997 Umbria-Marche (central Italy) seismic sequence, *Geophys. Res. Lett.*, doi:10.1029/2004GL022256, in press.

Beeler, N. M., R. W. Simpson, D. A. Lockner, and S. H. Hickman (2000), Pore fluid pressure, apparent friction and Coulomb failure, *J. Geophys. Res.*, *105*, 25,533–25,554.

Belardinelli, M. E., M. Cocco, O. Coutant, and F. Cotton (1999), Redistribution of dynamic stress during coseismic ruptures: evidence for fault interaction and earthquake triggering, *J. Geophys. Res.*, *104*, 14,925–14,945.

Caskey, S. J., and S. G. Wesnousky (1997), Static stress change and earthquake triggering during the 1954 Fairview Peak and Dixie Valley earthquakes, central Nevada, *Bull. Seismol. Soc. Am.*, *87*, 521–527.

Chiarabba, C., and A. Amato (2003), V_p and V_p/V_s images in the M_w 6.0 Colfiorito fault region (central Italy): A contribution to the understanding of seismotectonic and seismogenic processes, *J. Geophys. Res.*, *108*(B5), 2248, doi:10.1029/2001JB001665.

Chiaraluce, L., W. L. Ellsworth, C. Chiarabba, and M. Cocco (2003), Imaging the complexity of an active normal fault system: The 1997 Colfiorito (central Italy) case study, *J. Geophys. Res.*, *108*(B6), 2294, doi:10.1029/2002JB002166.

Chiaraluce, L., et al. (2004), Complex normal faulting in the Apennines thrust-and-fold belt: The 1997 seismic sequence in central Italy, *Bull. Seismol. Soc. Am.*, *94*, 99–116.

Chiodini, G., F. Frondini, C. Cardellini, and L. Peruzzi (2000), Rate of diffuse carbon dioxide Earth degassing estimated from carbon balance of regional aquifers: The case of central Apennine, Italy, *J. Geophys. Res.*, *105*, 8423–8434.

Cocco, M., and J. R. Rice (2002), Pore pressure and poroelasticity effects in Coulomb stress analysis of earthquake interactions, *J. Geophys. Res.*, *107*(B2), 2030, doi:10.1029/2000JB000138.

Cocco, M., C. Nostro, and G. Ekström (2000), Static stress changes and fault interaction during the 1997 Umbria-Marche earthquake sequence, *J. Seismol.*, *4*, 501–516.

Collettini, C., L. Chiaraluce, S. Pucci, M. R. Barchi, and M. Cocco (2005), Looking at fault inversion matching structural geology and seismology data, *J. Struct. Geol.*, in press.

Console, R., C. Montuori, and M. Murru (2000), Statistical assessment of seismicity patterns in Italy: are precursors or subsequent events?, *J. Seismol.*, *4*, 435–449.

Deschamps, A., et al. (2000), Spatio-temporal distribution of seismic activity during the Umbria-Marche crisis, *J. Seismol.*, *4*, 377–386.

Ekström, G., A. Morelli, E. Boschi, and A. M. Dziewonski (1998), Moment tensor analysis of the central Italy earthquake sequence of September–October 1997, *Geophys. Res. Lett.*, *25*, 1971–1974.

Hardebeck, J. L., J. J. Nazareth, and E. Hauksson (1998), The static stress change triggering model: Constraints from two southern California aftershock sequences, *J. Geophys. Res.*, *103*, 24,427–24,452.

Harris, R. A. (1998), Introduction to special section: stress triggers, stress shadows, and implications for seismic hazard, *J. Geophys. Res.*, *103*, 24,347–24,358.

Hernandez, B., M. Cocco, F. Cotton, S. Stramondo, O. Scotti, F. Courboulex, and M. Campillo (2004), Rupture history of the 1997 Umbria-Marche (central Italy) largest earthquakes from inversion of GPS, DInSAR and near field seismological data, *Ann. Geophys.*, *47*, 1355–1376.

Hodgkinson, K. M., R. S. Stein, and G. C. P. King (1996), The 1954 Rainbow Mountain-Fairview Peak-Dixie Valley earthquakes: A triggered normal faulting sequence, *J. Geophys. Res.*, *101*, 25,459–25,471.

Kilb, D., M. Ellis, J. Gomberg, and S. Davis (1997), On the origin of diverse aftershock mechanisms following the 1989 Loma Prieta earthquake, *Geophys. J. Int.*, *128*, 557–570.

King, G. C. P., and M. Cocco (2001), Fault interaction by elastic stress changes: new clues from earthquake sequences, *Adv. Geophys.*, *44*, 1–38.

King, G. C. P., R. S. Stein, and J. Lin (1994), Static stress change and the triggering of earthquakes, *Bull. Seismol. Soc. Am.*, *84*, 935–953.

Lavecchia, G., F. Brozzetti, M. Barchi, M. Menichetti, and J. V. A. Keller (1994), Seismotectonic zoning in east-central Italy deduced from analysis of the Neogene to present deformations and related stress fields, *Geol. Soc. Am. Bull.*, *106*, 1107–1120.

Mariucci, M. T., A. Amato, and P. Montone (1999), Recent tectonic evolution and present stress in the northern Apennines (Italy), *Tectonics*, *18*, 108–118.

McCloskey, J., S. S. Nalbant, S. Steacy, C. Nostro, O. Scotti, and D. Baumont (2003), Structural constraints on the spatial distribution of aftershocks, *Geophys. Res. Lett.*, *30*(12), 1610, doi:10.1029/2003GL017225.

Miller, S. A., C. Collettini, L. Chiaraluce, M. Cocco, M. R. Barchi, and B. J. P. Kaus (2004), Aftershocks driven by a high pressure CO_2 source at depth, *Nature*, *427*, 724–727, doi:10.1038/nature02251.

Nalbant, S. S., A. Hubert, and G. C. P. King (1998), Stress coupling between earthquakes in northwest Turkey and the north Aegean Sea, *J. Geophys. Res.*, *103*, 24,469–24,486.

Noir, J., E. Jacques, S. Bekri, P. M. Adler, P. Tapponier, and G. C. P. King (1997), Fluid flow triggered migration of events in the 1989 Dobi earthquake sequence of central Afar, *Geophys. Res. Lett.*, *24*, 2335–2338.

Nostro, C., M. Cocco, and M. E. Belardinelli (1997), Static stress changes in extensional regimes: An application to southern Apennines (Italy), *Bull. Seismol. Soc. Am.*, *87*, 234–248.

Okada, Y. (1985), Surface deformation due to shear and tensile faults in a half-space, *Bull. Seismol. Soc. Am.*, *75*, 1135–1154.

Okada, Y. (1992), Internal deformation due to shear and tensile faults in a half-space, *Bull. Seismol. Soc. Am.*, *82*, 1018–1040.

Papadimitriou, E., and L. R. Sykes (2001), Evolution of the stress field in the northern Aegean Sea (Greece), *Geophys. J. Int.*, *146*, 747–759.

Pino, N. A., S. Mazza, and E. Boschi (1999), Rupture directivity of the major shocks in the 1997 Umbria-Marche (central Italy) sequence from regional broadband waveforms, *Geophys. Res. Lett.*, *26*, 2101–2104.

Seeber, L., and J. G. Armbruster (2000), Earthquakes as beacons of stress change, *Nature*, *407*, 69–72.

Segall, P., and J. R. Rice (1995), Dilatancy, compaction, and slip instability of a fluid infiltrated fault, *J. Geophys. Res.*, *100*, 22,155–22,171.

Shapiro, S. A., R. Patzig, E. Rothert, and J. Rindshwentner (2003), Triggering of seismicity by pore-pressure perturbations: Permeability-related signature of the phenomenon, *Pure Appl. Geophys.*, *160*, 1051–1066.

Steacy, S., D. Marsan, S. S. Nalbant, and J. McCloskey (2004), Sensitivity of static stress calculations to the earthquake slip distribution, *J. Geophys. Res.*, *109*, B04303, doi:10.1029/2002JB002365.

Stein, R. S. (1999), The role of stress transfer in earthquake occurrence, *Nature*, *402*, 605–609.

Toda, S., and R. Stein (2003), Toggling of seismicity by the 1997 Kagoshima earthquake couplet: A demonstration of time-dependent stress transfer, *J. Geophys. Res.*, *108*(B12), 2567, doi:10.1029/2003JB002527.

Troise, C., G. De Natale, F. Pingue, and S. M. Petrazzuoli (1998), Evidence for static stress interaction among earthquakes in south-central Apennines (Italy), *Geophys. J. Int.*, *134*, 809–817.

D. Baumont and O. Scotti, Institut de Radioprotection et de Suretè Nuclèaire, Fontenay-Aux-Roses, France.

L. Chiaraluce, M. Cocco, and C. Nostro, Istituto Nazionale di Geofisica e Vulcanologia, via di Vigna Murata, 605, I-00143 Rome, Italy. (nostro@ingv.it)